

Texture descriptors by a fractal analysis of three-dimensional local coarseness

Florindo, Joao Batista; Landini, Gabriel; Bruno, Odemir Martinez

DOI:

[10.1016/j.dsp.2015.03.013](https://doi.org/10.1016/j.dsp.2015.03.013)

License:

Creative Commons: Attribution-NonCommercial-NoDerivs (CC BY-NC-ND)

Document Version

Peer reviewed version

Citation for published version (Harvard):

Florindo, JB, Landini, G & Bruno, OM 2015, 'Texture descriptors by a fractal analysis of three-dimensional local coarseness', *Digital Signal Processing*, vol. 42, pp. 70-79. <https://doi.org/10.1016/j.dsp.2015.03.013>

[Link to publication on Research at Birmingham portal](#)

Publisher Rights Statement:

After an embargo period this article is subject to the terms of a Creative Commons Attribution Non-Commercial No Derivatives license

Checked September 2015

General rights

Unless a licence is specified above, all rights (including copyright and moral rights) in this document are retained by the authors and/or the copyright holders. The express permission of the copyright holder must be obtained for any use of this material other than for purposes permitted by law.

- Users may freely distribute the URL that is used to identify this publication.
- Users may download and/or print one copy of the publication from the University of Birmingham research portal for the purpose of private study or non-commercial research.
- User may use extracts from the document in line with the concept of 'fair dealing' under the Copyright, Designs and Patents Act 1988 (?)
- Users may not further distribute the material nor use it for the purposes of commercial gain.

Where a licence is displayed above, please note the terms and conditions of the licence govern your use of this document.

When citing, please reference the published version.

Take down policy

While the University of Birmingham exercises care and attention in making items available there are rare occasions when an item has been uploaded in error or has been deemed to be commercially or otherwise sensitive.

If you believe that this is the case for this document, please contact UBIRA@lists.bham.ac.uk providing details and we will remove access to the work immediately and investigate.

Texture descriptors by a fractal analysis of three-dimensional local coarseness

Joao Batista Florindo^{a,*}, Gabriel Landini^a, Odemir Martinez Bruno^b

^a*Oral Pathology Unit, School of Dentistry, University Of Birmingham,
St Chad's Queensway, Birmingham, B4 6NN, United Kingdom*

^b*Instituto de Física de São Carlos (IFSC), Universidade de São Paulo
Av. Trabalhador São Carlense, 400, 13560-970 - São Carlos, SP, Brasil
phone/fax: +55 16 3373 8728 / +55 16 3373 9879*

Abstract

This work proposes a new method of extracting texture descriptors from digital images based on local scaling properties of the greyscale function using constraints to define connected local sets. The texture is first mapped onto a three-dimensional cloud of points and the local coarseness under different scales is assigned to each point p . This measure is obtained from the size of the largest “connected” set of points within a cube centred at p . Here, the “connected set” is defined as the set of points such that for each point in the local domain there is at least one other point at a distance smaller than a threshold t . Finally, the Bouligand-Minkowski fractal descriptors of the local coarseness of each pixel are computed. The classificatory power of the descriptors on the **Brodatz**, **Vistex**, **UIUC** and **UMD** databases showed an improvement over the results obtained with other well-known texture descriptors reported in the literature. The performance achieved also suggests possible applications to real-world problems where the images are best analysed as textures.

Keywords: Pattern Recognition, Fractal Descriptors, Local Connectivity,
Image Analysis

1. Introduction

There have been several fractal-based methods proposed for the analysis of complexity in images, including the analysis of image textures [1, 2, 3, 4, 5, 6, 7].

*Corresponding author
Preprint submitted to Elsevier
Email addresses: jbfiorindo@gmail.com (Joao Batista Florindo), January 26, 2015
G.Landini@bham.ac.uk (Gabriel Landini), bruno@ifsc.usp.br (Odemir Martinez Bruno)

15 Fractal geometry in image analysis has also found practical applications in a
16 number of areas [8, 9, 10, 44, 11, 12, 13, 14].

17 In a “texture image”, the analysis is typically focused on the statistical and
18 geometrical relations amongst pixel intensity patterns in different regions and
19 scales. In this context, fractal analysis becomes a powerful tool to address the
20 problem of measuring the complexity or the homogeneity of the texture across
21 scales. A pattern can be expressed by certain type of homogeneity at a partic-
22 ular resolution and here is where fractal geometry provides a straightforward
23 procedure to detect and relate such properties. Moreover, real world objects
24 commonly have some degrees of intrinsic self-similarity and therefore they might
25 be more suitably represented as approximations to fractal objects rather than to
26 regular Euclidean ones. Some of the successful fractal-based approaches tested
27 in this field include “multiscale fractal dimension” [15], multifractals [16] and
28 “fractal descriptors” [17]. Particularly, the latter has demonstrated to be highly
29 efficient for the discrimination of general textures [18, 19, 20, 13, 14, 21].

30 Here, we propose an alternative way of extracting texture descriptors based
31 on fractal geometry. The texture descriptors are computed using the Bouligand-
32 Minkowski fractal descriptors [20] based on the local coarseness of each pixel
33 [22, 23] rather than on the image intensity values [20, 17, 19]. The proposed
34 procedure performs a two-level complexity analysis. In the local domain, the
35 coarseness describes the clustering (or homogeneity) of the pixel neighbourhood,
36 while globally, the fractal descriptors represent the distribution of connectivities
37 across the image. These two complementary types of information appear to be
38 fundamental in describing and discriminating texture patterns at varying scales
39 in a more straightforward way than other statistical or geometrical solutions
40 proposed. Some advantages of the suggested approach are:

- 41 • A large number of real-world scenes (like those described by the textures
42 analysed here) have fractal-like characteristics;
- 43 • The “fractal properties” of textures are most often not homogeneous across
44 scales as expected with ideal fractal objects but the fractal descriptors

45 enable the quantification of such variability across the image;

- 46 • The local coarseness provides information about pixel neighbourhoods,
47 which is rather richer than pixel intensity alone.

48 The method performance was assessed on four well-known image databases
49 (Brodatz [24], Vistex [25], UIUC [33] and UMD [16]) and the results were com-
50 pared to other texture descriptors reported in the literature (Gabor [26], Fourier
51 [27], Grey-Level Cooccurrence Matrix (GLCM) [28], Multifractal [16], Local Bi-
52 nary Patterns (LBP) [29], Soft-LBP [35], Fuzzy-LBP [36] and textons (VZ)
53 [34]).

54

55 2. Related Works

56 Since the seminal work of Mandelbrot [42], several fractal-based methods
57 have been proposed in the literature to analyse texture images, and particularly
58 for the problem of texture classification. The most state-of-the-art and success-
59 ful approaches can be essentially divided into three categories: texton-based,
60 multifractals and fractal descriptors.

61 Texton (also called bag-of-words) methods follow the general scheme pre-
62 sented in [34]. The basic idea in this approach is to associate a vector of mea-
63 sures (texton or “word”) to each pixel or region of interest in the image and
64 cluster them into a number of groups (dictionary). Therefore, for each image
65 in the training and testing database, a model is built by using the histogram
66 of pixels whose corresponding textons are closer to a particular group in the
67 dictionary.

68 An example of texton-based fractal method is illustrated in [37], where the
69 image is submitted to a filter bank as in [34] and the textons are estimated by
70 the local fractal dimension of each filter response, computed by using the expo-
71 nential relation between the sum of pixel intensities within a neighbourhood of
72 the reference pixel and the radius of such neighbourhood. The remaining proce-

73 dures are classical in texton-based methods [34], involving K-means clustering
74 of textons and classification by nearest neighbours with χ^2 distance.

75 The second group of fractal-based methods includes the multifractal spec-
76 trum, which quantifies the distribution of a regularity parameter (the Holder
77 exponent) within local neighbourhoods of each image pixel. In [40] and [16]
78 the neighbourhood regularity is quantified by using a similar procedure to that
79 employed in [37], that is, the power-law relation between the sum of the pixel
80 intensities after Gaussian filtering within a neighbourhood and the radius of the
81 neighbourhood. The image is therefore partitioned into subsets, based on the
82 values of the local Holder exponents, and the texture features are given by the
83 box-counting dimension of each subset.

84 A more elaborated method to compute the local regularity is described in
85 [41], using wavelet leaders. A wavelet leader is the maximum response of a
86 wavelet decomposition inside a scale-space neighbourhood, that is, the neigh-
87 bourhood in this case is three-dimensional, including not only all the adjacent
88 points in the decomposition level as usual, but also those correspondent points in
89 neighbour scales in the wavelet pyramid. The use of wavelet leaders attenuates
90 one of the main problems with wavelet transforms, which is the large number of
91 small coefficients obtained for natural images. Another novelty in this method,
92 compared to [16], is the use of a multi-orientation approach to the image, to
93 overcome the orientation sensitivity of the wavelet transform. A more complete
94 version, including an adaptation to dynamic textures can be found in [38].

95 Multifractal methods can be further divided into dense and sparse approaches.
96 In dense methods, the Holder exponent is computed at each pixel in the image.
97 This is the case of the above methods. Another strategy is the sparse approach,
98 where the dimension is computed only over particular regions rather than over
99 all the pixels as proposed in [39]. In that case, the orientation histograms of
100 the scale-invariant gradient of the image is used to partition the image for the
101 posterior computation of the multifractal spectrum.

102 Finally, the third category of fractal methods in texture classification is
103 composed of the fractal descriptors, originally proposed in [17]. They employ

the values of the power-law curve associated to the fractal modelling to provide the image features in a straightforward manner. One of the most investigated approaches in this category are the Bouligand-Minkowski descriptors [20], where the texture is mapped onto a three-dimensional cloud of points and all the points are simultaneously dilated by spheres with radius r . The descriptors are obtained from the total volumes of the dilted cloud with various values of r . More details are given in Section 4.2. These features have been used either directly [20] or after some post-processing procedure [19]. Another variant is described in [18], where the entropy of the fractal descriptors are computed under different scales to accomplish the classification task.

The proposed method can be considered as part of the third group, although the local connectivity can also be associated to the concept of local regularity as employed in the multifractal spectrum. In a sense, it is similar to the multifractal approach, as both rely on a two-layer analysis: first, a local quantification of regularity (here expressed by the connectivity dimension), and second, a global distribution of such property. However, our proposal replaces the box-counting dimension of partition sets by the Bouligand-Minkowski descriptors. Such descriptors provide a more descriptive representation as, more than estimating the local dimension in the spatial domain of the image, they also reveal how the local regularity behaves across multiple scales. Moreover, the connectivity is also locally scale-invariant, which makes it a type of density function and allows the generation of descriptors robust to invariances in illumination changes, as discussed in [16].

3. Fractal Geometry

A fractal is a mathematical object with self-similarity (i.e. parts are similar to the whole) and typically high complexity (i.e. persistence of distinguishable details at various scales).

Same as Euclidean geometry defines fundamental measures such as area and perimeter, fractal geometry defines its own measures, one of the most important being the “fractal dimension”. This measures how the complexity (or space

134 occupation) of the object changes with changes of observational scale. Its value
 135 can be obtained from the general expression:

$$D = \lim_{\epsilon \rightarrow 0} \frac{\log(\mathfrak{M}(\epsilon))}{\log(\epsilon)}, \quad (1)$$

136 where $\mathfrak{M}(\epsilon)$ is a self-similarity measure which grows with the scale ϵ following
 137 a power law.

138 Despite mathematical fractals being ideal constructs, many seemingly self-
 139 similar and complex objects are easily found in the real world. In this context,
 140 there is vast literature on modelling real-world problems through fractal geom-
 141 etry and quantifying important properties using fractal dimensions. Applying
 142 fractal theory to digitised images requires to redefine the fractal dimension in a
 143 discrete and finite space, and several methods have been developed for this pur-
 144 pose [30, 31]. Two of these will be discussed below, the Bouligand-Minkowski
 145 and local connected dimension.

146 3.1. *Bouligand-Minkowski*

147 This method estimates the dimension of binary objects, but it can be straight-
 148 forwardly extended to grey-level textures [20].

149 The grey-level image is considered as a cloud of points in the three-dimensional
 150 Euclidean space, such that a pixel in the coordinate (x, y) and with intensity z
 151 is mapped onto a point with coordinates (x, y, z) . Then, each point in the cloud
 152 is morphologically dilated by spheres with radius r and the volume $V(r)$ of the
 153 dilated cloud is computed. The dimension is given by:

$$D = 3 - \alpha, \quad (2)$$

154 where α is the slope of the linear regression of $\log(V(r))$ on $\log(r)$.

155 3.2. *Local Connected Dimension*

156 The Local Connected Dimension [22] has been applied to binary images. As
 157 shown in Section 4 we use an adapted version for grey-scale images. This consist
 158 of computing a local dimensional value relative to each possible position of the

analysis, i.e. for each image pixel. Given a pixel p , within a local neighbourhood of size r_{max} , its local dimension $D_C(p)$ can be obtained by counting the number N of pixels connected (using, for example, 8-neighbour pixel connectivity in the plane) to p within a square window with side-length r always centred at p . When r is varied, the dimension is given by:

$$D_C(p) = \alpha_C, \quad (3)$$

where α_C is the slope of the linear regression of $\log(N(r))$ on $\log(r)$.

3.3. Bouligand-Minkowski Fractal Descriptors

While the fractal dimension has been shown to be useful in a variety of applications, it still is a single number, and this might be insufficient to model complex or heterogeneous objects. To take advantage of fractal geometry without being bound to a single number, the authors in [17] proposed using “fractal descriptors”, i.e. to use all the values from $\log(\mathfrak{M}(\epsilon))$ rather than their scaling relation. More specifically, they used the $\log(V(r))$ curve from Bouligand-Minkowski dimension to provide powerful features for texture image. These features can be used directly, after transformation, or combined (for instance, using different colour channels [21] or image windows [18]) and have been successfully used in texture analysis [18, 19, 20, 13, 14, 21].

4. Proposed Method

We propose a new method to compute fractal descriptors based on adapting the local connectivity concept to grey-level images to describe local patterns in images. Such adaptation essentially consists of mapping the image onto a three-dimensional cloud (considering the grey-level of the pixel as the third dimension) and replacing the concept of “adjacency” by that of “an Euclidean distance smaller than a threshold”.

183

184 4.1. Local Connectivity

185 The local fractal dimension has been used before to estimate the structure of
 186 binary sets. This is based on the local scaling of mass (binary pixels) using the
 187 mass-radius dimension and repeating the analysis to small regions, relative to a
 188 centre point position which can be repeated for many (or all) possible positions
 189 in an image. This method can be constrained to “local connected set” rather
 190 than just local sets by considering only the mass that is “locally connected” to
 191 the origin of the analysis. Such an approach was successfully applied in [22] to
 192 characterise the structure of retinal vessel patterns and to cancer and pre-cancer
 193 invasive patterns [9]. That approach, however, can be modified to accommodate
 194 non-binary sets (i.e. other image types). Here we consider the scaling of pixel
 195 intensities in grey-scale images as if they were embedded in a three-dimensional
 196 Euclidean space defined by the image coordinates and the intensity scale.

197 Based on this approach, the connectivity concept can be redefined by replac-
 198 ing the adjacency contact relation with a new connectedness property based on
 199 a three-dimensional Euclidean distance satisfying a predefined threshold.

200 To achieve this, the grey-level image $I : [1, M] \times [1, N] \rightarrow \mathfrak{R}$ is mapped into
 201 a cloud of points S in a three-dimensional Euclidean space, such that each x
 202 and y coordinate pairs are the coordinates of each pixel and the z coordinate is
 203 the respective pixel intensity.

$$S = \{(x, y, z) | I(x, y) = z\} \quad (4)$$

204 Following the mapping, a connectivity measure is computed for each point
 205 p in the cloud by considering a cube C_p^r with side-length r centred at the point:

$$C_p^r = \{(x, y, z) | x \in [x_p - r, x_p + r], y \in [y_p - r, y_p + r], z \in [z_p - r, z_p + r]\} \quad (5)$$

206 The connectivity measure $M_p^{r,t}$ is given by the number of points inside C_p^r
 207 and connected to p . Given that the concept of connectivity in three dimensions
 208 is not so straightforward as in two, here a connectivity based on Euclidean
 209 distances is employed. In this context, the set $\mathfrak{C}_p^{r,t}$ of points connected to p is a

subset of points within C_p^r such that each element has at least one other point
at a distance smaller than t within the cube.

$$\mathfrak{C}_p^{r,t} = \{p\} \cup \{p_i | p_i \in C_p^r \text{ and } \exists p_j \in C_p^r | D(p_i, p_j) < t\}, \quad (6)$$

where D is the three-dimensional Euclidean distance.

An optimized algorithm to find the connected components maps the points
in the cube into a non-weighted graph $G(V, E)$ such that:

$$v \in V \text{ iff } p_v \in C_p^r, \quad (7)$$

$$e_{i,j} \in E \text{ iff } \{p_i, p_j\} \subseteq C_p^r \text{ and } D(p_i, p_j) < t, \quad (8)$$

and then searches for the connected component of $G(V, E)$ that includes p .

The connectivity measure $M_p^{r,t}$ is given by the size (number of vertices) of
the connected component $\mathfrak{C}_p^{r,t}$. Figure 1 illustrates the connected components in
two dimensions to facilitate visualization. Figure 1(a), (b), (c) and (d) show the
steps for a window (two-dimensional version of the cube) with growing length r .
In each iteration the border of the current window is highlighted in black. Inside
the current window all the points at a distance smaller than t are connected by
an edge. Such process generates a graph with multiple connected components.
The points taking part into the connected component that contains the centre
pixel p are painted red. The connectivity of p (for each r) is given by the number
of red points inside the respective window.

In a similar way to the analysis of binary images, to characterise the scaling
of local connectivity in grey-scales, a local Holder exponent can be computed
by:

$$\alpha(p) = \lim_{r \rightarrow 0} \frac{\log(M_p^{r,t})}{\log(r)}. \quad (9)$$

Given that the range of r cannot be made large enough to estimate the relation
with confidence, the limit loses part of its significance and the coarse (or coarse-
grained) Holder exponent [23] arises as a more interesting measure. This is
given by:

$$\alpha_r(p) = \frac{\log(M_p^{r,t})}{\log(r)}. \quad (10)$$

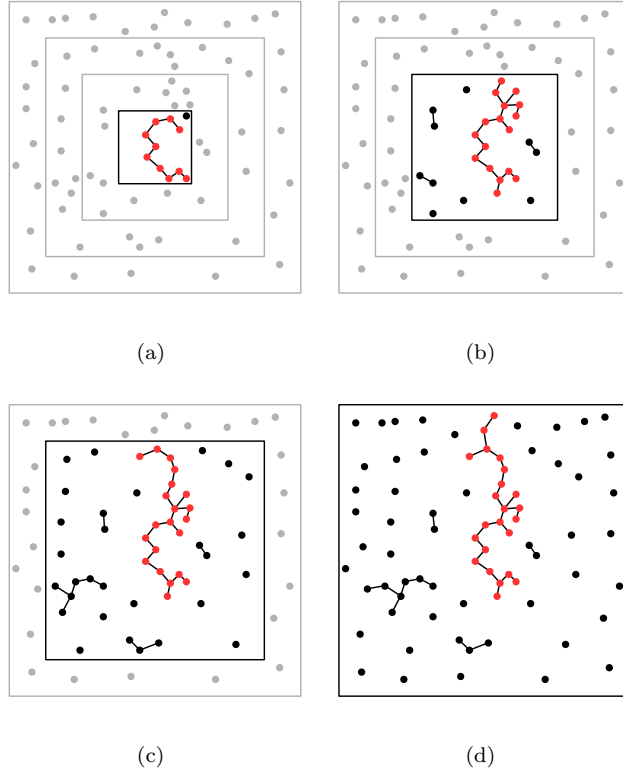


Figure 1: Computing the connectivity of a pixel p (centre point). (a), (b), (c) and (d) exemplify the process for different window lengths. Inside the current window (highlighted in black) all the points at a distance smaller than t are connected by an edge resulting in a multi-component graph. The connectivity is given by the number of points in the connected component containing the centre point (these are painted red).

234 The threshold t is an empirically pre-defined value. After computing α_r for
 235 each pixel, the procedure ends up with a matrix of values M_{α_r} for each r . Here,
 236 the values of r were varied between 1 and 6, with t ranging between 1 and 10.

237 Finally, the Bouligand-Minkowski fractal descriptors are computed over each
 238 one of the six matrices M_{α_r} (one for each value of r) and concatenated to provide
 239 the final texture descriptors.

240

241 4.2. Bouligand-Minkowski Descriptors

242 The procedure to compute the Bouligand-Minkowski descriptors of each ma-
 243 trix consists of two steps. First, each point in the matrix is mapped onto a
 244 three-dimensional cloud of points. Second, all the points in the cloud are si-
 245 multaneously dilated by a sphere with radius r and the total volume $V(r)$ of
 246 the dilated cloud is computed. The descriptors correspond to the values of
 247 $V(r)$ when r ranges within a pre-defined range. More details are given in the
 248 following.

249 At first, the real-valued matrix $M_{\alpha_r} : [1, W] \times [1, H] \rightarrow \mathfrak{R}$, where W is the
 250 width and H the height of the matrix, is mapped onto a three-dimensional cloud
 251 of points C . Such mapping is obtained by associating each point in M_{α_r} with
 252 coordinate $(x, y) \in ([1, W] \times [1, H])$ and such that $M(x, y) = z$, $z \in \mathfrak{R}$, with a
 253 point with coordinates $(x, y, z) \in C$.

254 In the following, each point in C is dilated by a radius r , and the total volume
 255 $V(r)$ of the dilated cloud is computed. In practice, all the points are replaced
 256 by a sphere with radius r and, depending on the value of r and the distance
 257 among the points in the cloud, such spheres can touch and merge. Therefore,
 258 the total dilated volume is not just the sum of the volumes of the individual
 259 spheres, but it encloses relevant information about the distribution of points in
 260 the cloud and, as a consequence, the distribution of α_r in M .

261 Particularly, when $V(r)$ is analysed within a range of values of r , it provides a
 262 useful insight about the homogeneity of α_r . If such distribution is homogeneous,
 263 the cloud C is regular and the curve $\log r \times \log V(r)$ is similar to a straight line.
 264 If, on the other hand, such coefficients are distributed in an irregular way on M ,

there is a larger number of values of r for which new collisions arise and thus the log – log curve is more irregular as well. Such behaviour of $V(r)$ is what makes it appealing to summarize the information expressed by the local coarseness.

The total volume $V(r)$ of the dilated cloud corresponds to the number of points pertaining to the union of spheres $B(p, r)$ centred at each point $p \in C$ with radius r :

$$V(r) = \sum_{p'} \mathbf{1}_U(p'), \quad (11)$$

being $\mathbf{1}$ the indicator function ($\mathbf{1}_U(p') = 1$ if $p' \in U$ and 0, otherwise) and

$$U = \bigcup_{p \in C} B(p, r). \quad (12)$$

272

In practice, an efficient way to compute $V(r)$ is by using the Euclidean Distance Transform (EDT), given that the set $B(p, r)$ in the above expression contains the points at a distance at most r from p . In a three-dimensional space, the EDT of a point p' is provided by:

$$EDT(p') = \min_{p \in C} (\mathbf{dist}(p, p')), \quad (13)$$

where $\mathbf{dist}(p, p')$ is the Euclidean distance between the points. More details on methods to compute the EDT efficiently can be found in [43].

The Bouligand-Minkowski descriptors $\mathfrak{D}(u)$ are obtained by computing the EDT over all points within a region of interest around C . Those EDT values are thus increasingly sorted into a vector o and the descriptors correspond to the logarithm of the cumulated number of points p' such that $EDT(p') \leq o(u)$:

$$\mathfrak{D}(u) = \log \left[\sum_{i=1}^u \delta(EDT(p') - o(u)) \right], \quad (14)$$

where δ is the unit response function ($\delta(x) = 1$, if $x = 0$, and $\delta(x) = 0$, otherwise). The index u corresponds to the non-negative values of the EDT within the region of interest. For example, for $r \leq 2$ there are 4 possible values for u (1, $\sqrt{2}$, $\sqrt{3}$ and 2), and thus 4 descriptors are computed. Here we use $r \leq 10$, providing 85 descriptors.

288 As the number of descriptors can become very large in most cases, a Prin-
 289 cipal Component Analysis is performed after the concatenation. The following
 290 algorithm express each step in a pseudo-code language, while Figure 2 synthe-
 291 sizes these steps on a diagram. That diagram shows the steps involved in the
 292 proposed method, sequentially from top to bottom. First of all, a grey level
 293 image is depicted, following by the matrices M_{α_r} , represented as intensity im-
 294 ages for r between 1 and 6. After that, the Bouligand-Minkowski descriptors
 295 are computed for each previous matrix, providing the exhibited log – log curves.
 296 Finally, at the bottom, the Bouligand-Minkowski **descriptors** are concatenated
 297 and submitted to a Principal Component Analysis with the aim of reducing the
 298 dimensionality. It is worth noting that M_{α_r} behaves like a multiscale transform
 299 over the texture where increasing values of r gradually “smooth” details, since
 300 points falling inside a same cube are expected to have similar Holder coarseness.

```

301  for  $r = 1$  until 6 do
302      for all  $p \in I$  do
303          for all  $q_1 \in C_r^p$  do
304              for all  $q_2 \in C_r^p \wedge q_2 \neq q_1$  do
305                  if  $\text{distance}(q_1, q_2) \leq t$  then
306                       $\text{add}(G, \{q_1, q_2\})$ 
307                  end if
308              end for
309          end for
310           $\mathfrak{C}_p^{r,t} \leftarrow \text{findConnectedComponent}(G, p)$ 
311           $M_{\alpha_r}(p) \leftarrow \frac{\log(|\mathfrak{C}_p^{r,t}|)}{\log(r)}$ 
312      end for
313       $D^r \leftarrow \text{BouligandMinkowskiDescriptors}(M_{\alpha_r})$ 
314  end for
315   $D \leftarrow \text{concatenate}(D^1, D^2, D^3, D^4, D^5, D^6)$ 
316   $\text{descriptors} \leftarrow \text{PCA}(D)$ 

```

Figure 3 shows how the proposed descriptors can precisely classify some textures from Brodatz database. Even with only a few PCA scores the classes can be distinguished. It is still worth stressing that although using more components causes the curves approximate each other, as they less contribute to the variability, those components when put together allow higher precision when managed by efficient classifiers. Such promising results are consequence of combining the measure of complexity under different perspectives: the first (Holder coarseness) more local and focused on the pixel neighbourhood, the second (Bouligand-Minkowski) more global, expressing how the topology of the texture is defined. The complementary information given by both provides a richer method to well characterize even the most complex and irregular textures.

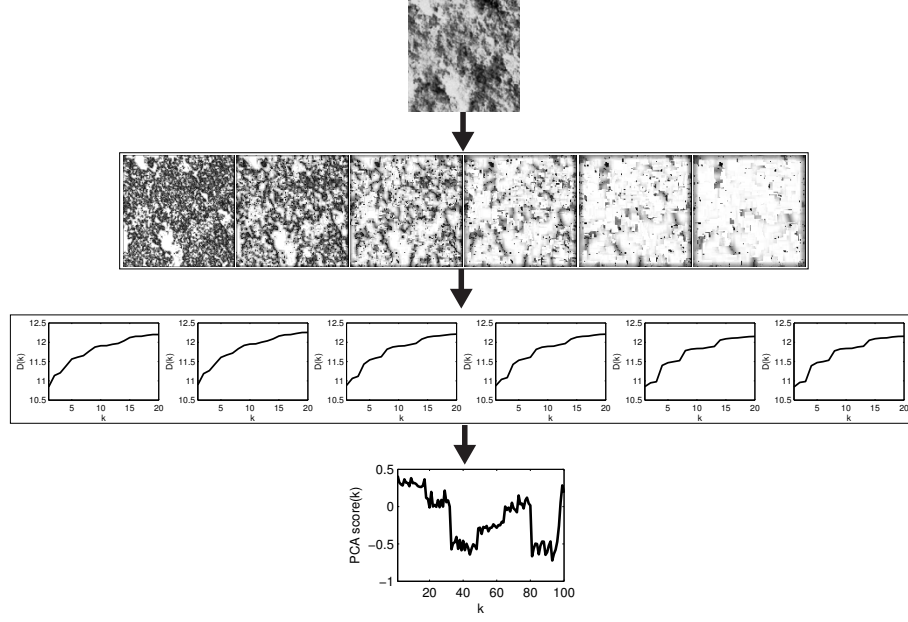


Figure 2: Steps in the proposed method. At the top, the grey-level texture to be analysed. Below, the M_{α_r} matrices expressing the coarseness at each pixel in the original image, with $r \in [1, 6]$, represented in an intensity image. In the following row, the respective Bouligand-Minkowski curves computed over each M_{α_r} is exhibited and finally the concatenated descriptors after applying a Principal Component Analysis are shown at the bottom of the diagram.

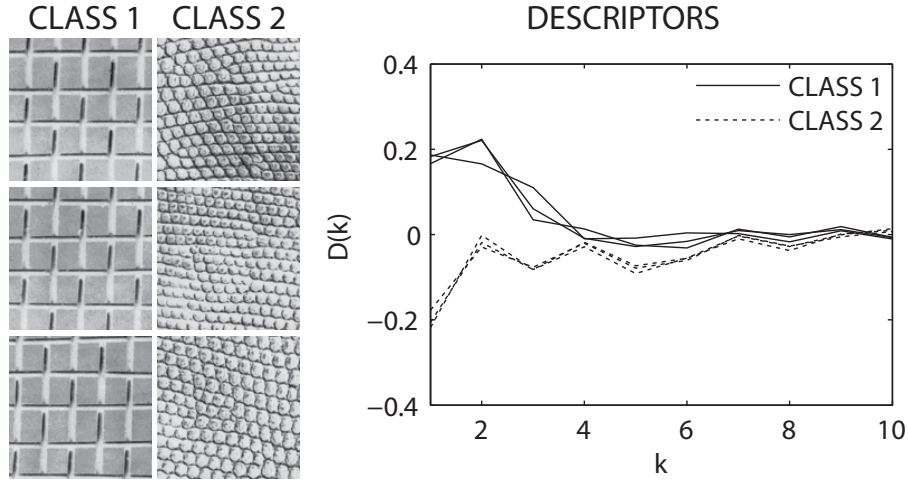


Figure 3: First PCA scores ($D(k)$) of the proposed descriptors from images of two classes (objects). The groups can be identified by the descriptors even visually.

328 5. Experiments

329 The performance of our approach was tested against other well-known tex-
330 ture descriptors to classify four benchmark databases (Brodatz [24], Vistex [25],
331 UIUC [33] and UMD [16]).

332 The Brodatz database is a collection of grey-scale images from photos of an
333 architectural textures book [24]. One hundred and eleven images were used,
334 with each one being split into 16 non-overlapping windows, resulting in 111
335 classes with 16 samples each.

336 The Vistex database is a classical texture image collection [25] composed
337 by colour images with different resolutions. Images of size 512×512 pixels
338 were converted to grey-level textures and split into 16 non-overlapping windows,
339 resulting in 54 classes with 16 samples each.

340 For the UIUC database we use a more recent version employed in [33], com-
341 posed by 25 classes with 40 grey-level samples per class and each sample has a
342 resolution of 256×256 pixels.

343 The forth database is UMD [16], composed by 25 classes with 40 grey-level
344 images in each one and each image has a high resolution of 1280×960 . To speed
345 up the computation, here a downsampled version was employed and each image
346 has a 256×192 resolution.

347 The total number of descriptors depends on the maximum radius of the
348 Bouligand-Minkowski dilation. Table 1 shows this relation, although in most
349 cases, a reduced number of descriptors were enough to obtain the success rates
350 reported here. The numbers used in practice are discussed in Section 6.

351 The descriptors were computed for each image and the results were compared
352 (in terms of precision over a cross-validation classification of each database) with
353 other classical and state-of-the-art approaches, to know, (Gabor [26], Fourier
354 [27], Grey-Level Cooccurrence Matrix (GLCM) [28], Multifractal [16], Local
355 Binary Patterns (LBP) [29], Soft-LBP [35], Fuzzy-LBP [36] and textons (VZ)
356 [34]).

357 The classification was carried out through a Linear Discriminant Analysis

Table 1: Total number of descriptors for each radius used by the Bouligand-Minkowski dilation.

Dilation radius	Number of descriptors
1	6
2	24
3	48
4	84
5	132
6	186
7	252

using a 10-fold scheme for cross-validation [32]. The precision (named “Success Rate” in Results section), in this case, corresponds to the average percentage of images correctly classified in each round of the cross-validation procedure, according to the ground-truth provided by each database.

6. Results and Discussions

6.1. Parameter settings

The cube side-lengths considered to compute the connected components and therefore the Holder exponent were fixed between 1 and 6, as greater values became computationally unfeasible on standard hardware. For the threshold t , larger values were thought to provide more information as they produced larger components, however, distances greater than 10 were, again, computationally costly. Moreover, the use of larger values of t tends to make the coarseness measures quite similar along the neighbourhood and such local homogeneity would impair the ability of fractal descriptors to detect small-scale patterns in the texture.

The remaining variable to establish was the dilation radius in the Bouligand-Minkowski analysis. Table 2 shows the success rates of classification (as a percentage) for a number of dilation radii and the number of fractal descriptors

376 generated for Brodatz data set. This was done to identify radii values pro-
 377 viding best performance with a minimum number of descriptors (and avoid
 378 over-training issues such as dimensionality curses).

Table 2: Success rates of classification and number of descriptors for different dilation radii on the Brodatz database.

Dilation radius	Success rate (%)	Number of descriptors
1	69.93	6
2	87.67	23
3	91.16	48
4	91.95	73
5	92.12	105
6	92.40	138
7	92.74	242

379 The same test and results on the Vistex database are shown in Table 3, for
 UIUC in Table 6.1 and for UMD in Table 6.1.

Table 3: Success rates of classification and number of descriptors for different dilation radii on the Vistex database.

Dilation radius	Success rate (%)	Number of descriptors
1	62.74	6
2	89.59	23
3	91.44	33
4	93.87	73
5	95.03	132
6	95.14	118
7	95.60	142

380

381 From the results above, we concluded that 6 was a reasonable value for the
 382 dilation radius as it produces a number of descriptors similar to those used in
 383 other established methods while outperforming them in the rates of classification
 384 obtained.

Table 4: Success rates of classification and number of descriptors for different dilation radii on the UIUC database.

Dilation radius	Success rate (%)	Number of descriptors
1	59.10	6
2	73.30	24
3	81.70	48
4	86.80	65
5	87.90	112
6	89.50	124
7	90.10	229

Table 5: Success rates of classification and number of descriptors for different dilation radii on the UMD database.

Dilation radius	Success rate (%)	Number of descriptors
1	66.90	5
2	81.50	19
3	86.40	47
4	90.80	83
5	93.10	116
6	94.00	150
7	93.90	178

385 6.2. Classification

386 The graphs and tables below show the results obtained by the proposed
 387 method as well as the performance of other approaches. Figure 4 shows the
 388 success rates on the Brodatz database according to the number of descriptors
 389 used. Most methods show a rapid increase in the correct classification rates as
 390 the number of descriptors increase, then reaching a stability level. While our
 391 method does not produce the best performance with few descriptors it shows
 392 the best performance when these are 25. Furthermore the performance increase
 appears to be smoother than for the other methods, too.

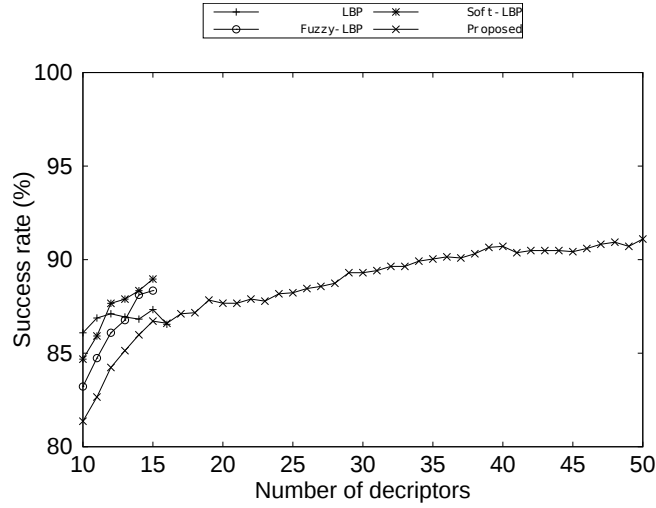


Figure 4: Success rates of classification and number of descriptors for various methods applied to the Brodatz database.

393

394 Table 6 shows the best classification results achieved for each method in
 395 the previous graph, the number of descriptors necessary to reach such rate and
 396 the associated cross-validation error. Except for the classical Fourier approach,
 397 the other methods have similar performances (around 86%), while however our
 398 proposed method achieved nearly 92% (a notable improvement, given the size
 399 and complexity of the textures database).

400 Figure 5 shows another very useful and helpful way of evaluating the per-
 401 formance of a classifier, i.e, the confusion matrix. This diagram aims to show

Table 6: Success classification rates (with the respective errors) and number of descriptors for various methods applied to the Brodatz database.

Method	Success rate (%)	Number of descriptors
LBP	87.33 \pm 0.02	15
GLCM	86.48 \pm 0.02	70
Multifractal	85.64 \pm 0.03	70
Gabor	85.42 \pm 0.02	19
Fourier	78.71 \pm 0.03	15
Fuzzy LBP	88.34 \pm 0.02	15
Soft LBP	88.96 \pm 0.02	15
Textons	81.47 \pm 0.02	97
Proposed	91.84 \pm 0.01	96

the number of elements from the class A (expected) that were assigned to the class B (predicted). The elements that are correctly classified are represented in the diagonal, while the number of misclassified samples can be inferred from the outside. Here the values on the diagonal are expressed by grey-levels (the darker the point, the higher the number of samples), whilst those outside are depicted in red levels only to facilitate the visualization. In this type of representation, an ideal classifier is expected to have the maximum possible of dark points on the diagonal and the minimum in the outside. In Figure 5, as supposed, the best methods in this visual sense are LBP and the proposed descriptors. However, although they behave in a similar way in some cases like the confused samples around the class 40, the proposed fractal descriptors exhibits less dark red points confirming the higher correctness rate and identifying the classes where more or less samples can be distinguished.

Figure 6 shows the classification rates for the Vistex database. The relative results are similar to those for Brodatz, although the curves here are more irregular; this is likely due to a more pronounced variation in patterns amongst the images.

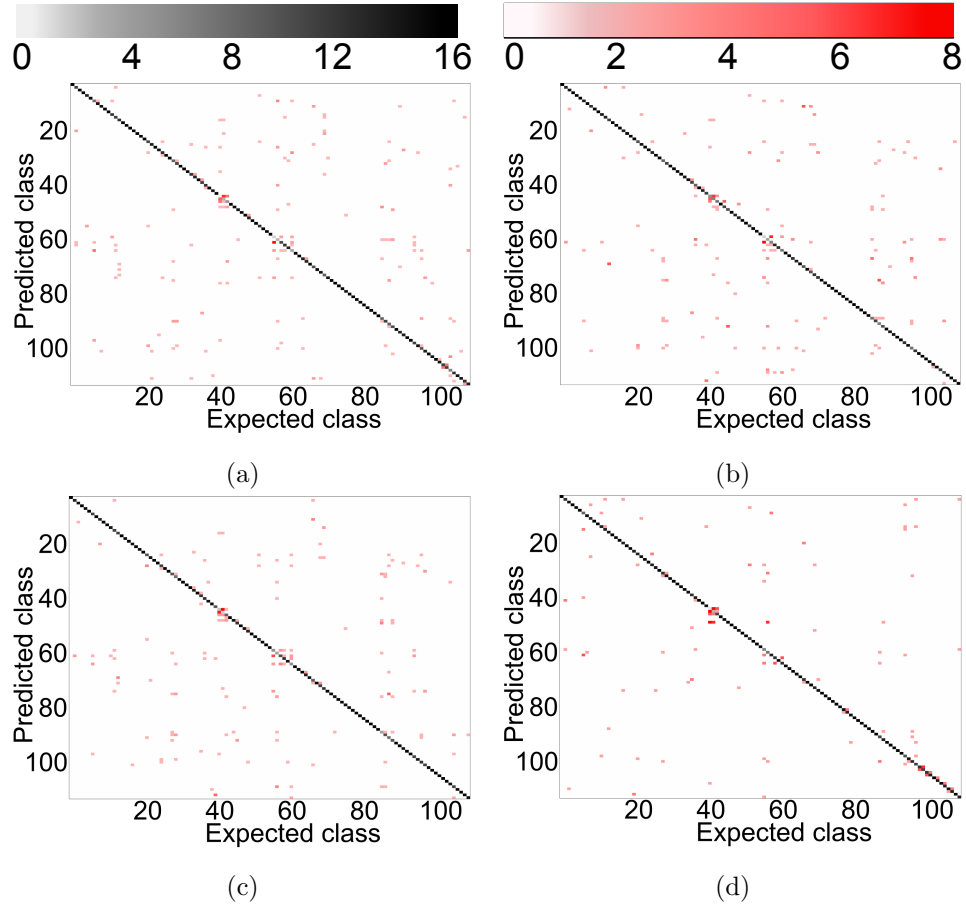


Figure 5: Confusion matrices for the methods on Brodatz data set. (a) LBP. (b) Fuzzy-LBP. (c) Soft-LBP. (d) Proposed method.

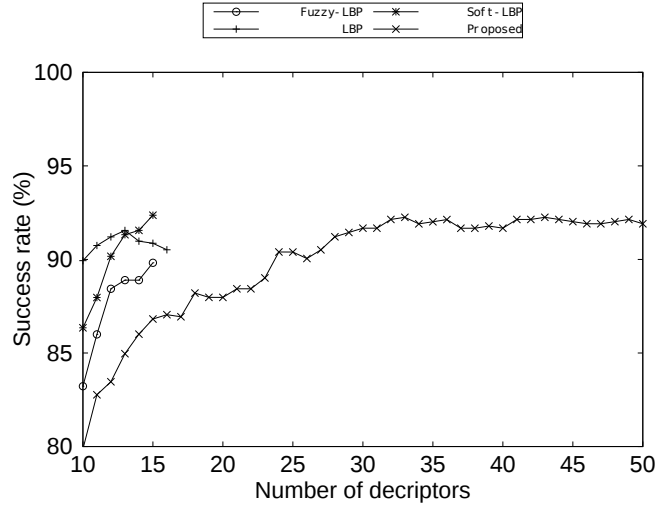


Figure 6: Success classification rates and number of descriptors for the Vistex database.

Table 7 shows the percentage of images correctly classified in Vistex database. The reduced number of classes appears to benefit the performance of the methods, as the rates are greater than for the Brodatz database results. Again, the proposed method demonstrates its potential in the analysis of complex textures; the Vistex images contain a high level of heterogeneity caused by shadows, orientation, scale, etc. However, the combination of local and global multiscale analysis in the the proposed method achieved about 94.5% correct classification.

Figure 7 shows the confusion matrices for Vistex in the same scheme used for Brodatz. Despite the difference in appearance with the matrices for the analysis of the Brodatz textures (which have fewer classes, Figure 5), the proposed descriptors correctly identifies more classes. Apart from the reduced number of red points, this also can be observed by a diagonal more continuous, with less grey gaps. Moreover, the classification errors are not concentrated at any specific classes, ensuring higher reliability to the method for a practical application.

Figure 8, Table 8 and Figure 9 show the results for the classification of UIUC database, following the same scheme adopted for the previous databases,

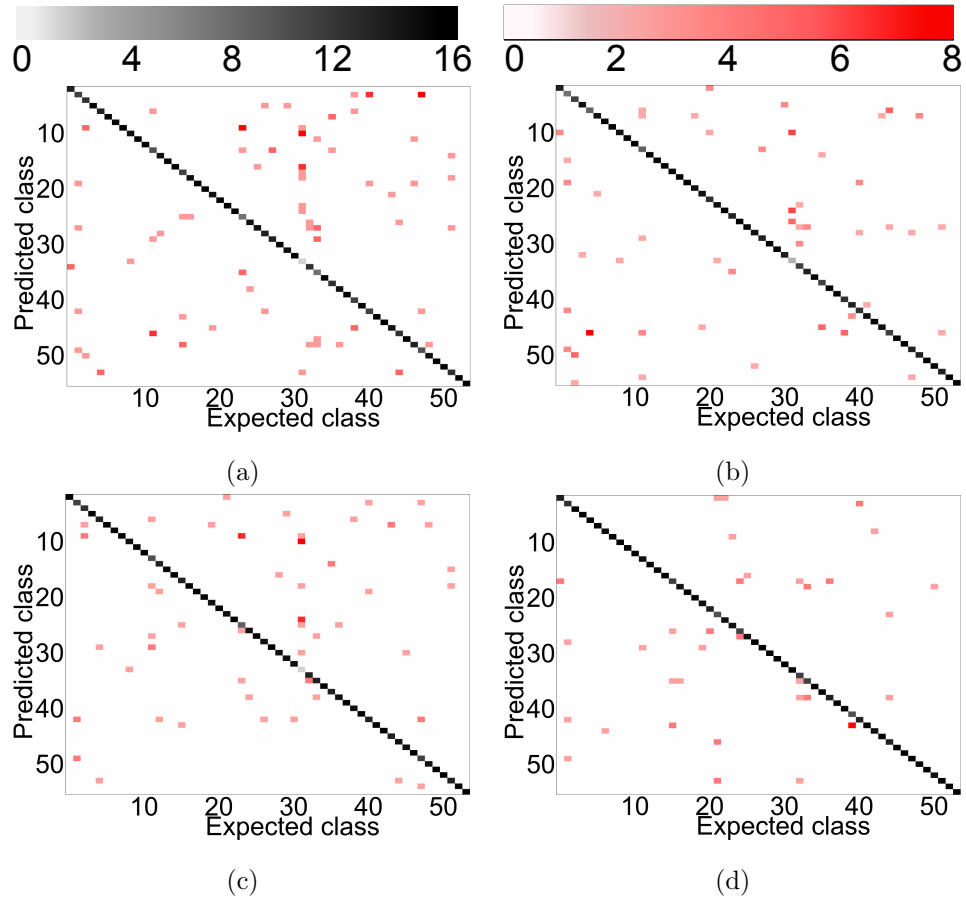


Figure 7: Confusion matrices for the methods on Vistex data set. (a) Fuzzy-LBP. (b) LBP. (c) Soft-LBP. (d) Proposed method.

Table 7: Success classification rates (with respective errors) and number of descriptors for various methods applied to the Vistex database.

Method	Success rate (%)	Number of descriptors
LBP	91.55±0.03	13
GLCM	88.21±0.03	70
Multifractal	88.31±0.03	76
Gabor	90.39±0.01	17
Fourier	84.49±0.02	15
Fuzzy LBP	89.82±0.04	15
Soft LBP	92.36±0.03	15
Textons	86.00±0.02	98
Proposed	94.45±0.02	74

that is, success rate against number of descriptors, highest success rates and confusion matrices. An interesting point to be observed in this case is that methods like LBP and variants, which provided good results in the classification of Vistex and Brodatz, now present results below the average. The main cause of such discrepancy are the significant changes in viewpoint, scale and illumination conditions on UIUC samples. Approaches like classical LBP (and its variants) and GLCM focus their analysis on grey-levels and local neighbourhood, whereas their global descriptors are not complex and precise enough to identify a global change in albedo for example. On the other hand, multifractals and textons, using, respectively, local measures invariant to illumination and multiple types of filters, were capable of identify samples even when they are presented under different perspectives and distances from the observer. Finally, the proposed method again achieved the highest percentage of images correctly classified. Such performance is a consequence, as stated before, of the efficiency of combining two complementary local and global fractal analysis, addressing the respective variations amongst samples from the same class by means of descriptors that quantify the local regularity as well as the texture

454 patterns at each scale instead of using only the pixel intensities or ambiguous
 455 global measures like histograms or fractal dimension.

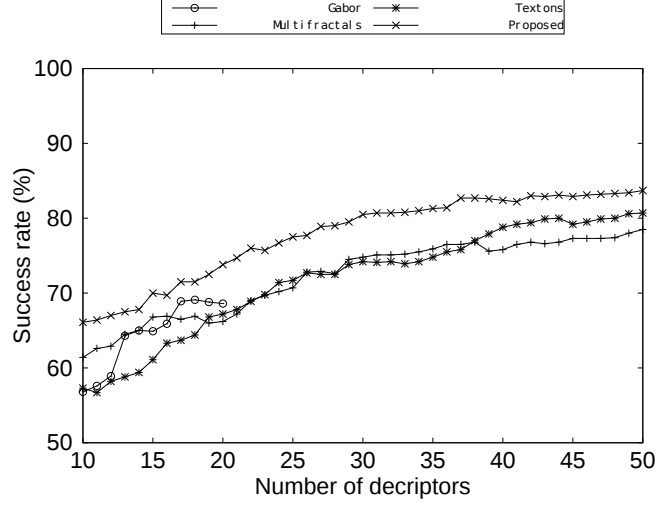


Figure 8: Success classification rates and number of descriptors for the UIUC database.

455

Table 8: Success classification rates (with respective errors) and number of descriptors for various methods applied to the UIUC database.

Method	Success rate (%)	Number of descriptors
LBP	57.80 ± 0.05	14
GLCM	58.70 ± 0.03	13
Multifractal	82.40 ± 0.03	70
Gabor	69.10 ± 0.03	18
Fourier	67.30 ± 0.03	10
Fuzzy LBP	51.60 ± 0.06	15
Soft LBP	54.90 ± 0.05	15
Textons	86.70 ± 0.03	97
Proposed	88.00 ± 0.02	85

456 Finally, Figure 10, Table 9 and Figure 11 exhibit the results for the classi-
 457 fication of UMD by the compared descriptors. A similar discussion to that for
 458 UIUC database is also valid here. In fact, UMD shares similarities with UIUC,

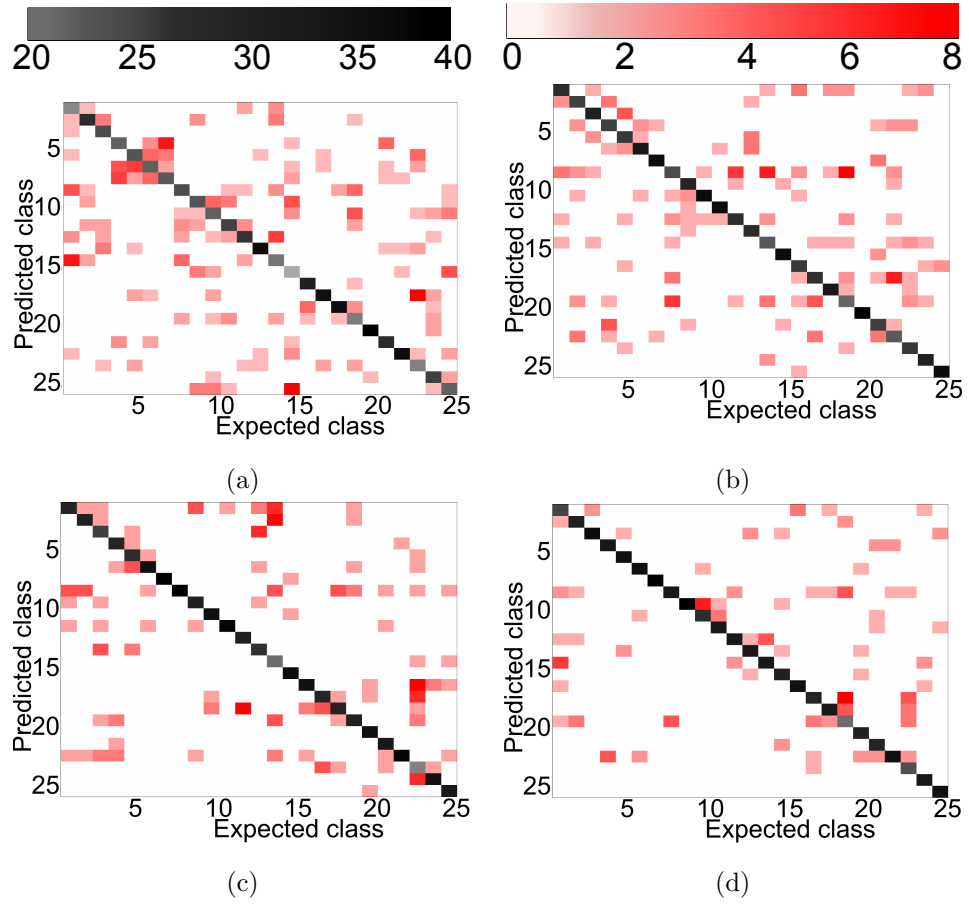


Figure 9: Confusion matrices for the methods on UIUC data set. (a) Gabor. (b) Multifractals. (c) Textons. (d) Proposed method.

mainly in their high variance of viewpoints and scales, in addition to the uncontrolled illumination conditions. The good results for multifractals was also expected since the database was proposed and employed in the corresponding paper ([16]). Another observation is that in Figure 10 multifractal descriptors outperformed the proposed method for a number of descriptors smaller than 50. This can also be explained by characteristics of the database and, particularly, by the complexity of the samples, containing, for instance, dozens of packets of wall anchors or tins of joint compound, each unit with complex labels attached. Even in this case, however, the proposed method provided the highest success rate when more than 80 descriptors were employed.

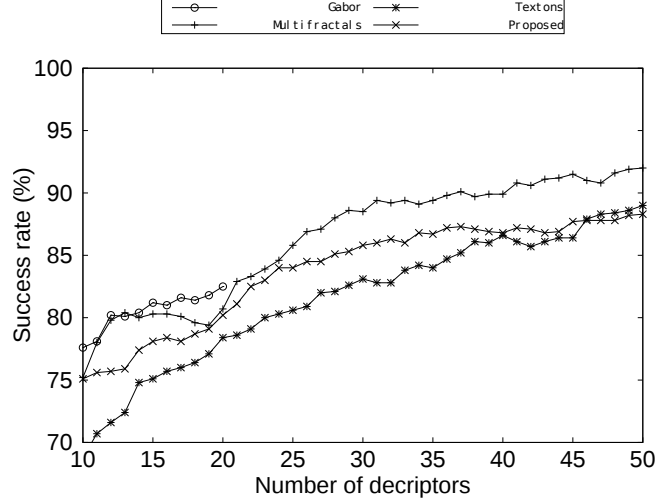


Figure 10: Success classification rates and number of descriptors for the UMD database.

468

Based on these results, we conclude that the combination of fractal descriptors and local coarseness Holder exponent allows a rich and precise description of complex and heterogeneous textures. One advantage of our method is that it analyses two domains. The first one is local and provides measures of the clustering of pixel neighbourhoods while the second, deals with the distribution of the clustering across the image, giving a measure of its homogeneity. Moreover, computing the coarseness at different cube sizes makes this procedure a multi-scale analysis. Furthermore, the fractal descriptors provide a detailed analysis

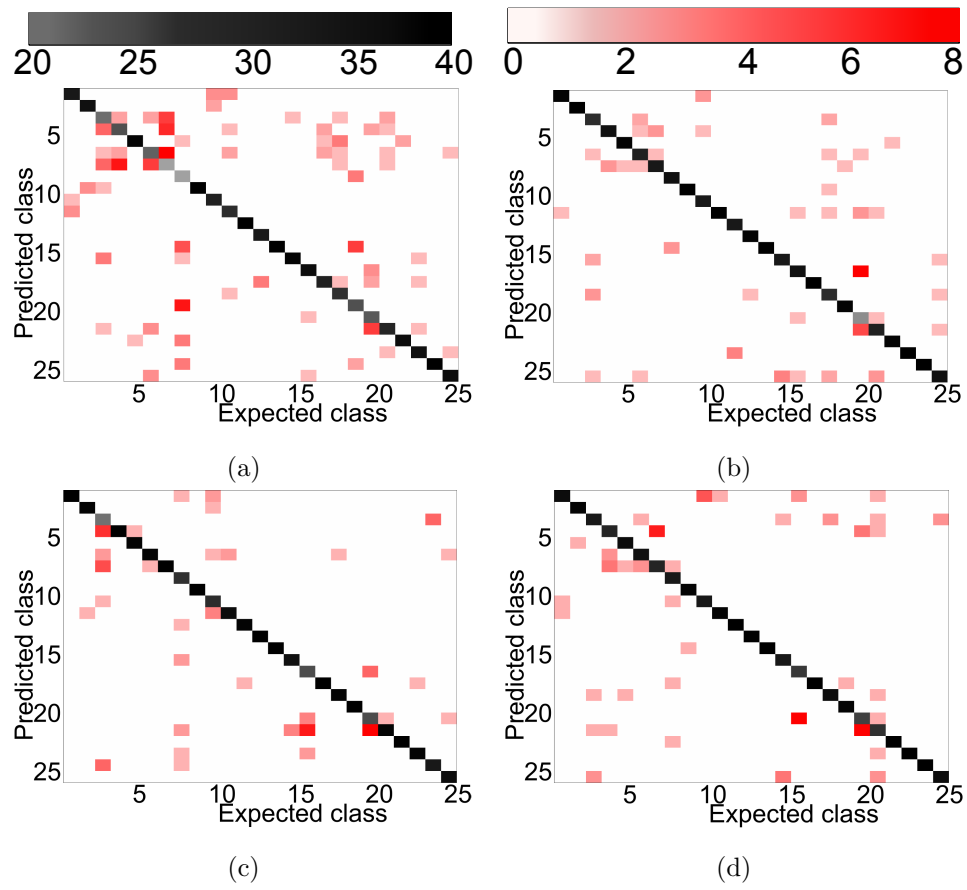


Figure 11: Confusion matrices for the methods on UMD data set. (a) Gabor. (b) Multifractals. (c) Textons. (d) Proposed method.

Table 9: Success classification rates (with respective errors) and number of descriptors for various methods applied to the UMD database.

Method	Success rate (%)	Number of descriptors
LBP	77.90 \pm 0.03	12
GLCM	78.20 \pm 0.04	16
Multifractal	92.10 \pm 0.03	72
Gabor	82.50 \pm 0.03	20
Fourier	75.50 \pm 0.02	15
Fuzzy LBP	78.20 \pm 0.03	15
Soft LBP	77.80 \pm 0.03	14
Textons	92.50 \pm 0.02	100
Proposed	93.00 \pm 0.02	100

477 in terms of the spatial distribution of such clustering measure.

478 We empirically identified that with regards to the local fractal measure of
479 natural images, the connectivity itself can also be characterised as self-similar (as
480 shown in [22]) while the Bouligand-Minkowski descriptors summarise how the
481 variation of such self-similarity occurs at the different scales analysed [20, 17].

482 The result of this double-level multiscale and fractal analysis (through frac-
483 tal descriptors and the local coarseness, respectively) leads to a set of quantifiers
484 that are perhaps more robust to abrupt texture variations. Such robustness is
485 a consequence of two main points: firstly, the local dimension is taken over a
486 neighbourhood, which attenuates the effect of a punctual irregularity (noise,
487 for example) in the pixel and, secondly, the fractal descriptors capture relevant
488 information at different scales and, hence, localised variations would not com-
489 promise the global performance of the descriptor to a large extent. The inherent
490 multiscale procedure also retains information about different levels of details in
491 the images, making possible a more precise and reliable classification.

492 7. Conclusions

493 We proposed a new method to extract texture descriptors from grey-level
494 images by computing the Bouligand-Minkowski fractal descriptors from a matrix
495 containing the coarseness Holder exponent (logarithm of the number of points
496 connected to each pixel in the original image).

497 The method was applied to classify well-known databases and the perfor-
498 mance compared to other classical and state-of-the-art texture analyses pub-
499 lished in the literature. Our method outperformed all other analyses for **the**
500 **compared** databases.

501 The results suggest that fractal descriptors and local coarseness exponent
502 provide complementary information about the textures. While the coarseness
503 index measures pixel clustering and consequently the neighbourhood homogene-
504 ity, the fractal descriptors provide a measure of the regularity of the distribution
505 of Holder exponents, and consequently the distribution of patterns along scales.
506 After removal of redundancies through PCA, the descriptors become a powerful
507 tool to represent and describe complex textures.

508 Acknowledgments

509 Odemir Martinez Bruno gratefully acknowledges the financial support of
510 CNPq (National Council for Scientific and Technological Development, Brazil)
511 (Grant Nos. 308449/2010-0 and 473893/2010-0) and FAPESP (Grant No.
512 2011/01523-1). Joao Batista Florindo acknowledges support from FAPESP
513 (The State of São Paulo Research Foundation) (Grant No. 2013/22205-3).

514 References

- 515 [1] J. Wang, N. Zheng, Y. Liu, G. Zhou, Parameter analysis of fractal im-
 516 age compression and its applications in image sharpening and smoothing,
 517 Signal Processing: Image Communication 28 (6) (2013) 681 – 687.
- 518 [2] H. Xiaoqing, Z. Qin, L. Wenbo, A new method for image retrieval based
 519 on analyzing fractal coding characters, Journal of Visual Communication
 520 and Image Representation 24 (1) (2013) 42 – 47.
- 521 [3] C.-W. Shih, H.-C. Chu, Y.-M. Chen, C.-C. Wen, The effectiveness of im-
 522 age features based on fractal image coding for image annotation, Expert
 523 Systems with Applications 39 (17) (2012) 12897 – 12904.
- 524 [4] X.-Y. Wang, Y.-X. Wang, J.-J. Yun, An improved no-search fractal image
 525 coding method based on a fitting plane, Image and Vision Computing 28 (8)
 526 (2010) 1303 – 1308.
- 527 [5] A. Napryushkin, V. Kibitkin, V. Pleshanov, Linear transformation based
 528 error correction algorithm for fractal dimension estimation of images, Signal
 529 Processing 90 (6) (2010) 2094 – 2101.
- 530 [6] M. Keyvanpour, F. Merrikh-Bayat, An effective chaos-based image water-
 531 marking scheme using fractal coding, Procedia Computer Science 3 (0)
 532 (2011) 89 – 95.
- 533 [7] J. Velzquez-Garca, K. Oleschko, J. A. Muoz-Villalobos, M. Velsquez-Valle,
 534 M. M. Menes, J.-F. Parrot, G. Korvin, M. Cerca, Land cover monitoring
 535 by fractal analysis of digital images, Geoderma 160 (1) (2010) 83 – 92.
- 536 [8] G. Landini, Fractals in microscopy, Journal of Microscopy 241 (1) (2011)
 537 1–8.
- 538 [9] G. Landini, J. W. Rippin, How important is tumour shape? quantification
 539 of the epithelial-connective tissue interface in oral lesions using local con-
 540 nected fractal dimension analysis, The Journal of Pathology 179 (2) (1996)
 541 210–7.

- 542 [10] P.-L. Lin, P.-W. Huang, C.-H. Lee, M.-T. Wu, Automatic classification
543 for solitary pulmonary nodule in {CT} image by fractal analysis based on
544 fractional brownian motion model, *Pattern Recognition* 46 (12) (2013) 3279
545 – 3287.
- 546 [11] J. xiang Du, C.-M. Zhai, Q.-P. Wang, Recognition of plant leaf image based
547 on fractal dimension features, *Neurocomputing* 116 (0) (2013) 150 – 156.
- 548 [12] Y. Wu, Q. Lin, Z. Chen, W. Wu, H. Xiao, Fractal analysis of the retrograda-
549 tion of rice starch by digital image processing, *Journal of Food Engineering*
550 109 (1) (2012) 182 – 187.
- 551 [13] J. B. Florindo, M. S. Sikora, E. C. Pereira, O. M. Bruno, Characterization
552 of nanostructured material images using fractal descriptors, *Physica A:
553 Statistical Mechanics and its Applications* 392 (7) (2013) 1694 – 1701.
- 554 [14] J. B. Florindo, N. R. da Silva, L. M. Romualdo, F. de Fátima da Silva, P. H.
555 de Cerqueira Luz, V. R. Herling, O. M. Bruno, Brachiaria species identi-
556 fication using imaging techniques based on fractal descriptors, *Computers
557 and Electronics in Agriculture* 103 (0) (2014) 48 – 54.
- 558 [15] E. T. M. Manoel, L. da Fontoura Costa, J. Streicher, G. B. Müller, Mul-
559 tiscale fractal characterization of three-dimensional gene expression data,
560 in: *SIBGRAPI*, IEEE Computer Society, 2002, pp. 269–274.
- 561 [16] Y. Xu, H. Ji, C. Fermüller, Viewpoint invariant texture description using
562 fractal analysis, *International Journal of Computer Vision* 83 (1) (2009)
563 85–100.
- 564 [17] O. M. Bruno, R. de Oliveira Plotze, M. Falvo, M. de Castro, Fractal dimen-
565 sion applied to plant identification, *Information Sciences* 178 (12) (2008)
566 2722–2733.
- 567 [18] J. B. Florindo, O. M. Bruno, Texture analysis by multi-resolution fractal
568 descriptors, *Expert Systems with Applications* 40 (10) (2013) 40224028.

- [19] J. B. Florindo, A. R. Backes, M. de Castro, O. M. Bruno, A comparative study on multiscale fractal dimension descriptors, *Pattern Recognition Letters* 33 (6) (2012) 798–806.
- [20] A. R. Backes, D. Casanova, O. M. Bruno, Plant leaf identification based on volumetric fractal dimension, *International Journal of Pattern Recognition and Artificial Intelligence* 23 (6) (2009) 1145–1160.
- [21] A. R. Backes, D. Casanova, O. M. Bruno, Color texture analysis based on fractal descriptors, *Pattern Recognition* 45 (5) (2012) 1984 – 1992.
- [22] G. Landini, P. I. Murray, G. P. Misson, Local connected fractal dimensions and lacunarity analyses of 60 degrees fluorescein angiograms, *Investigative Ophthalmology and Visual Science* 36 (13) (1995) 2749–2755.
- [23] H. Peitgen, H. Jürgens, D. Saupe, *Chaos and Fractals: New Frontiers of Science*, Springer, 2004.
- [24] P. Brodatz, *Textures: A photographic album for artists and designers*, Dover Publications, New York, 1966.
- [25] Vistex, Vistex. vision texture database (2009).
URL <http://vismod.media.mit.edu/vismod/imagery/VisionTexture/vistex.html>
- [26] B. Manjunath, W. Ma, Texture features for browsing and retrieval of image data, *IEEE Transactions on Pattern Analysis and Machine Intelligence* 18 (8) (1996) 837–842.
- [27] R. C. Gonzalez, R. E. Woods, *Digital Image Processing (2nd Edition)*, Prentice Hall, Upper Saddle River, 2002.
- [28] R. M. Haralick, Statistical and structural approaches to texture, *Proceedings of the IEEE* 67 (5) (1979) 786–804.

- [29] T. Ojala, M. Pietikäinen, D. Harwood, A comparative study of texture measures with classification based on featured distributions, *Pattern Recognition* 29 (1) (1996) 51–59.
- [30] K. Falconer, *Fractal Geometry: Mathematical Foundations and Applications*, Wiley, Chichester, UK, 2003.
- [31] J. C. Russ, *Fractal Surfaces*, Plenum Press, New York, 1994.
- [32] R. O. Duda, P. E. Hart, *Pattern Classification and Scene Analysis*, Wiley, New York, 1973.
- [33] K. Kilic, R. Abiyev, Exploiting the synergy between fractal dimension and lacunarity for improved texture recognition, *Signal Processing* 91 (10) (2011) 2332–2344.
- [34] M. Varma, A. Zisserman, A Statistical Approach to Texture Classification from Single Images, *International Journal of Computer Vision* 62 (1-2) (2005) 61 – 81.
- [35] T. Ahonen, M. Pietik, M. Pietikäinen, Soft histograms for local binary patterns, in: *Proceedings of the Finnish signal processing symposium*, IEEE, 2007, pp. 1–4.
- [36] D.K. Iakovidis, E.G. Keramidas, D. Maroulis, Fuzzy Local Binary Patterns for Ultrasound Texture Characterization, in: *Image Analysis and Recognition*, Springer Berlin / Heidelberg, 2008, pp. 750–759.
- [37] M. Varma, R. Garg, Locally Invariant Fractal Features for Statistical Texture Classification, in: *IEEE 11th International Conference on Computer Vision*, IEEE, 2007, pp. 1–8.
- [38] H. Ji, X. Yang, H. Ling, Y. Xu, Wavelet Domain Multifractal Analysis for Static and Dynamic Texture Classification, *IEEE Transactions on Image Processing* 22 (1) (2013) 286 – 299.

- 620 [39] Y. Xu, S. Huang, H. Jib, C. Fermüller, Scale-space texture description
 621 on SIFT-like textons, *Computer Vision and Image Understanding* 116 (1)
 622 (2012) 999 – 1013.
- 623 [40] Y. Xu, H. Ji, C. Fermüller, A projective invariant for textures, in: *Com-*
 624 *puter Vision and Pattern Recognition*, IEEE, 2006, pp. 1932–1939.
- 625 [41] Y. Xu, X. Yang, H. Ling, H. Ji, A new texture descriptor using multifractal
 626 analysis in multi-orientation wavelet pyramid, in: *Computer Vision and*
 627 *Pattern Recognition*, IEEE, 2010, pp. 161–168.
- 628 [42] B. B. Mandelbrot, *The Fractal Geometry of Nature*, Freeman, New York,
 629 1982.
- 630 [43] R. Fabbri, L. Costa, J. Torelli, O. Bruno, 2D Euclidean distance transform
 631 algorithms: A comparative survey, *ACM Computer Surveys* 40 (1) (2008)
 632 1 – 44.
- 633 [44] R. A. Eid, G. Landini, Quantification of the global and local complexity
 634 of the epithelial-connective tissue interface of normal, dysplastic, and neo-
 635 plastic oral mucosae using digital imaging, *Pathology Research & Practice*
 636 199 (7) (2003) 475 – 482.